Peer reviewed version

Link to publication record in Explore Bristol Research
PDF-document

## University of Bristol - Explore Bristol Research
### General rights

# Oxygen Reduction at Carbon Supported Lanthanides: The Role of the B-site

Verónica Celorrio,[a] Ellie Dann, [a] Laura Calvillo,[b] David J. Morgan,[c] Simon R. Hall,[a] and David J. Fermín*[a]

**Abstract:** The kinetics of the oxygen reduction reaction (ORR) at carbon supported transition metal oxides in alkaline solutions is systematically investigated as a function of the nature of the B-site. The study is focused on $LaBO_3$ (B = Cr, Co, Fe, Mn and Ni) nanoparticles synthesized by an ionic liquid route, offering fine control over phase purity and composition. Activity towards the ORR was compared with commercial Pt/Etek catalyst. Detailed electrochemical analysis employing a rotating ring-disc electrode provides conclusive evidences that the carbon support plays an important contribution in the faradaic responses. Decoupling the contribution of the carbon support uncovers that the reactivity of $LaMnO_3$ towards the 4e- ORR pathway is orders of magnitude higher than for the other lanthanides. We rationalise these observations in terms of changes in the redox state at the B-site close to the formal oxygen reduction potential.

## Introduction

Oxygen reduction reaction (ORR) is one of the most challenging reactions in energy conversion devices such as fuel cells and metal air batteries.[1] In alkaline environment, it is generally considered that ORR can proceed *via* a four electron transfer to produce OH- (1), or *via* a two electron transfer to produce $HO_2^-$ (2).[2]

$$O_2 + 2H_2O + 4e^- \rightarrow 4OH^- \qquad (1)$$
$$O_2 + H_2O + 2e^- \rightarrow HO_2^- + OH^- \qquad (2)$$
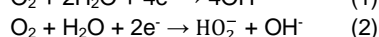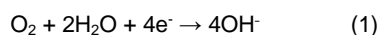
The generation of OH- from $HO_2^-$ can be achieved by either the redox step (3),

$$HO_2^- + H_2O + 2e^- \rightarrow 3OH^- \qquad (3)$$
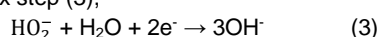
or the decomposition reaction (4)

$$2\,HO_2^- \rightarrow 2OH^- + O_2 \qquad (4)$$
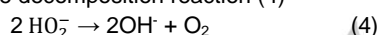
Platinum-based catalysts are often quoted as benchmark materials for the ORR in acid and alkaline environments,[3] while significant efforts have also been focused on earth abundant and low-cost materials.[4] Noble metal based catalysts are fundamentally limited by the so-called *scaling factors* arising from the fact that multiple intermediates are involved in the overall reaction.[5] On the other hand, transition metal oxides have been generating a lot of interest for fuel cells operating under neutral and high pH conditions.[6] Complex transition metal oxides are a huge family of compounds and the establishment of appropriate descriptors linking structure and reactivity is crucially important in this field.

Since the seminal work by Bockris and Otagawa in the 1980's,[7] the establishment of descriptors correlating electronic properties of perovskite oxides and their activities towards oxygen electrocatalysis have been subject of considerable debate. More recently, the elegant work by Suntivich *et al.* suggested that single electron occupancy of the $e_g$ orbital represents the optimum configuration for oxygen electrocatalysis.[8] These authors proposed empty $e_g$ orbitals leads to strong $B-O_2$ bonding, while fully occupied $e_g$ orbitals significantly weakens $O_2$ binding.[8b] DFT calculations also concluded that the adsorption strength of intermediates increases as the number of outer B-site valence electrons increases.[8a, 9]

Although these descriptors are conceptually simple and attractive, there are a number of issues which are not fully understood. Discussion mainly focuses on the strength of $B-O_2$ bonding, which may not necessarily be the rate determining factor in the 4-electron process. Furthermore, recent studies have provided compelling evidences that perovskites based oxide materials inherently exhibit A-site surface segregation after being prepared at high temperatures.[10] Burriel *et al.* demonstrated that the outer surface of $La_{2-x}Sr_xNiO_{4+\delta}$ single crystals is mainly (La, Sr)O terminated.[10b]

Another important aspect to consider is that many of these oxides are poor electronic conductors, requiring their dispersion in porous carbon films to improve charge transport. As the activity of these oxides is measured in alkaline solution, the contribution of the ORR reaction at the carbon surface (2-electron reaction) must be accounted for.[11] Hardin *et al.* reported that the addition of carbon to the electrode improved the activity of oxides for oxygen reduction, but not for oxygen evolution, concluding that carbon materials play a key role in the mechanism beyond charge transport.[12] The work by Poux *et al.* showed that carbon not only offers electrical contact to oxide nanoparticles, but also reduces $O_2$ to ($HO_2^-$). This process could be coupled to the reaction at the oxide material, which may lead to generation of OH- by either reactions (3) or (4).[6c, 13] Malkhandi *et al.* observed this synergetic

[a]     Dr V. Celorrio, Ms. E. Dann, Dr S.R. Hall, Dr D.J. Fermín*
        School of Chemistry
        University of Bristol
        Cantocks Close, Bristol BS8 1TS, UK
        E-mail: David.Fermin@bristol.ac.uk
[b]     Dr L. Calvillo
        Dipartimento di Scienze Chimiche
        Università di Padova
        Via Marzolo 1
        35131 Padova, Italy
[c]     Dr D.J. Morgan
        Cardiff Catalysis Institute, School of Chemistry
        Cardiff University
        Cardiff CF10 3AT, UK

        Supporting information for this article is given via a link at the end of the document.

effect investigating the activity of $La_{0.6}Ca_{0.4}CoO_{3-x}$ (LCCO) supported on acetylene black carbon.[14]

In the present work, we report an analysis of the ORR kinetics catalyzed by phase pure $LaCrO_3$, $LaMnO_3$, $LaFeO_3$, $LaCoO_3$ and $LaNiO_3$ nanoparticles supported on Vulcan XC-72R. These particles were prepared by a highly versatile ionic liquid method.[15] The reactivity of the carbon supported oxides was studied by rotating ring-disk electrodes (RRDE), monitoring the ratio between 4- and 2-electron mechanisms. Employing the model developed by Damjanovic *et al.*,[16] the phenomenological rate constants for the 4-electron process were estimated as a function of the electrode potential. Our studies show the reactivity of $LaMnO_3$ towards the 4-electron process is several orders of magnitude higher than for the other oxides. These observations do not appear to support *d*-orbital occupancy of the B-site as the key activity descriptor in these systems. We rationalize the higher activity of $LaMnO_3$ in terms of changes in the oxidation state of Mn (III) sites at potential close to the formal ORR potential. We discuss the nature of the active sites and propose an alternative approach to benchmark the reactivity of these materials.

## Results and Discussion

Figure 1 shows XRD data of the various oxide nanoparticles synthesized by the ionic liquid method. All of the diffractograms are characterized by a high phase purity judging from the match with reported standards. $LaMnO_3$ was indexed to the rhombohedral (R-3cH) phase which is consistent with an oxygen excess $\delta$. Stoichiometric $LaMnO_3$ has been reported featuring an orthorhombic crystal structure,[17] which is characterized by XRD patterns substantially different to those shown in figure 1. A quantitative analysis of the oxygen content based on XRD patterns is somewhat complex due to signal broadening introduced by the nanoscale dimensions of the crystalline domains. In the case of $LaMnO_{3+\delta}$, a significant splitting of the XRD peak between 32 and 34° can be observed for values of $\delta > 0.09$. Consequently, we expect the oxygen content below this level for the particles examined in this work. Having established this point, and for the sake of simplicity, we will be referring to this material as $LaMnO_3$ throughout this work. $LaFeO_3$ was indexed to the corresponding cubic (Pm3m) phase. $LaCrO_3$ exhibited the orthorhombic (Pbnm) phase, while $LaCoO_3$ and $LaNiO_3$ were assigned to the rhombohedral phase.
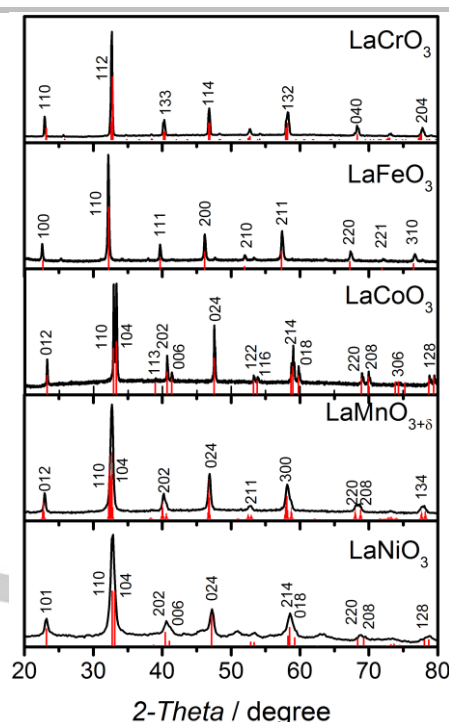


**Figure 1.** XRD of $LaCrO_3$, $LaFeO_3$, $LaCoO_3$, $LaMnO_{3+\delta}$ and $LaNiO_3$. Red vertical bars correspond to standard patterns JCPDS-ICDD File No. 01-071-1231, 01-075-0541, 00-048-0123, 01-073-8342 and 01-072-1241, respectively.

A representative SEM image of $LaNiO_3$ is shown in Figure 2, illustrating the characteristic morphology and microstructure of the synthesized oxide. EDX analysis of a section of the porous network reveals a homogeneous distribution of La (figure 2b) and Ni (figure 2c). Quantitative elemental analysis was also consistent with the material stoichiometry. These results, also observed for the other lanthanides (Supporting Information Figure S1), are consistent with the high phase purity revealed by XRD.
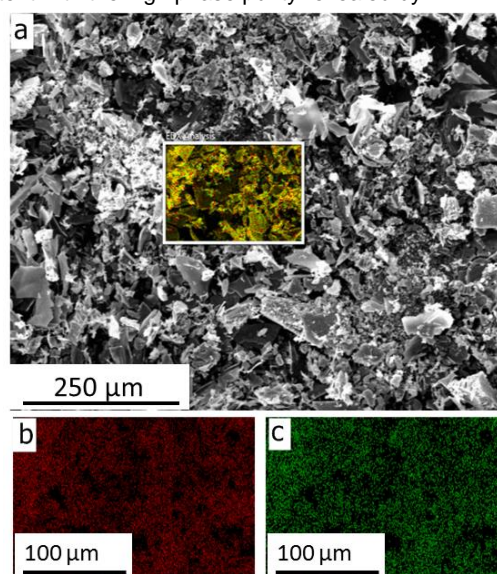


**Figure 2.** Representative SEM (a) micrograph of $LaNiO_3$, with the corresponding La (b) and Ni (c) elemental mapping.

Figures 3a and 3c show representative TEM images of LaMnO₃ and LaNiO₃, respectively, illustrating nanocrystals with mean particle sizes of 35 nm (TEM images of the other oxides can be found in Figure S2 of the supporting information). Particle size distributions (shown in figure S3) are relatively broad with LaMnO₃, LaNiO₃ and LaCoO₃ oxides exhibiting a mean diameter between 30 and 35 nm. Larger particles were obtained for LaFeO₃ (60 nm) and LaCrO₃ (195 nm). The larger particle size for the latter two oxides reflects, to a large extent, the fact that higher temperatures were required to promote phase purity. The lattice fringes observed in high resolution TEM images (figures 3b and 3d) demonstrate the high degree of crystallinity of the as-prepared oxides. The 0.27 nm d-spacing obtained for LaMnO₃ (fig. 3b) is consistent with the {110} planes. Figure 3b also shows that the size of the crystalline domains is comparable to the nanoparticle size. In the case of LaNiO₃ (figure 3d), the 0.38 nm spacing is linked to the {012} planes. HRTEM images of the other oxides can be found in the Supporting Information (Figure S4).
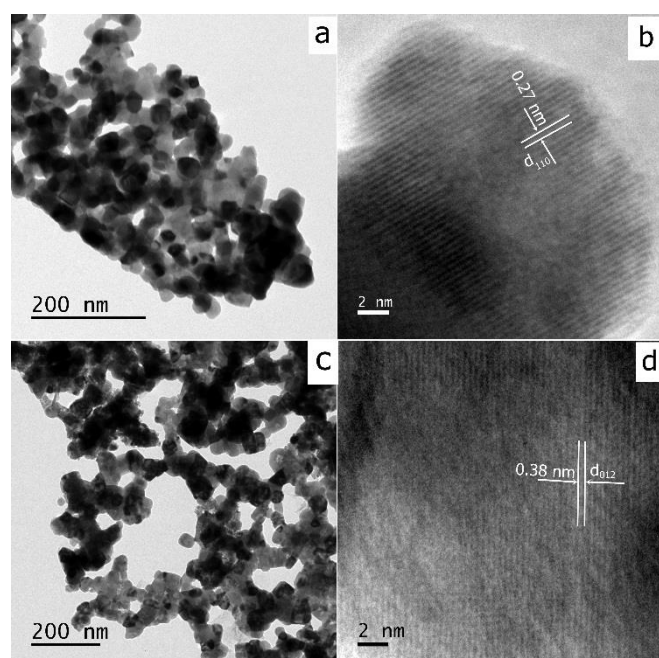


**Figure 3.** TEM and HRTEM images of as-synthesized LaMnO₃ (a, b) and LaNiO₃ (c, d).

XPS spectra of LaNiO₃, LaMnO₃, LaFeO₃ and LaCoO₃ are displayed in Figure 4, showing the La 3$d$, Ni 2$p$, Mn 2$p$, Fe 2$p$ and Co 2$p$ regions. La 3$d_{5/2}$ (833.5 - 835.1 eV) and La 3$d_{3/2}$ (850.3 - 851.9 eV) signals are split into two peaks each as a result of contributions from several initial and final states, with the La 3$d_{5/2}$ binding energy (BE) consistent with a La$^{3+}$ state.[18] The La 3$d$ line contains also the components associated with La₂O₃/La(OH)₃ (components at higher BEs) resulting from La surface segregation,[18c] which may be responsible for slight variations in the peak shape for the various oxides. The La 3$d_{3/2}$ peak overlaps with the main Ni 2$p_{3/2}$ peak, making difficult the accurate determination of the Ni 2$p$ BE and, therefore, the Ni oxidation state. However, the positions of the Ni 2$p_{3/2}$ satellite and Ni 2$p_{1/2}$ peaks at 861.4 and 872 eV, respectively, are in agreement with a

Ni$^{3+}$ state. The BEs of the Co 2$p_{3/2}$ (780.1 eV) and Fe 2$p_{3/2}$ (710.2 eV) peaks are also good indicators of 3+ oxidation state of the B-site. In addition, the Co 2$p$ line does not show the Co 2$p_{3/2}$ satellite peak at 786 eV, characteristic of Co$^{2+}$. The presence of a Fe 2$p_{3/2}$ satellite peak at 719 eV further supports the assignment to a Fe$^{3+}$ oxidation state. In the case of Mn 2$p_{3/2}$, BE associated with the oxidation states 4+ (642.2 eV) and 3+ (641.9 eV) are very difficult to resolve. However, taking into account the information obtained from XRD, electron microscopy and elemental analysis, we can conclude that the B-site oxidation state of all of the as-grown material is primarily +3.
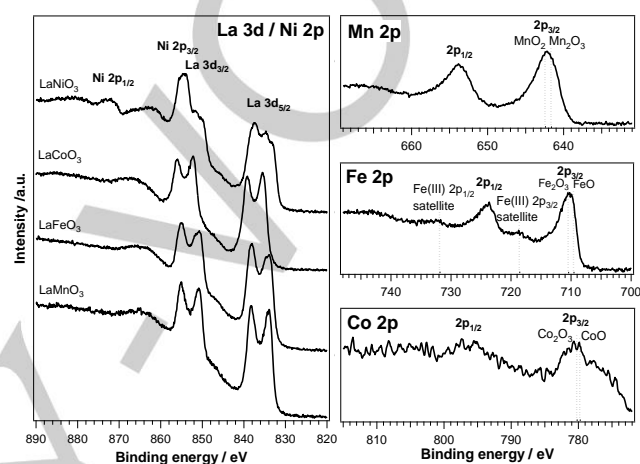


**Figure 4.** Characteristic XPS spectra of La 3$d$, Ni 2$p$, Mn 2$p$, Fe 2$p$ and Co 2$p$ core levels for LaNiO₃, LaMnO₃, LaFeO₃ and LaCoO₃.

La:B-site surface atomic ratios in the range of 2 to 5 were observed for this family of lanthanides, indicating a significant surface segregation of the A-site. Observations of La enriched surfaces are consistent with previous reports on other perovskite materials.[10a, 10b] This is rather significant in the case of LaCoO₃, which is responsible for the low signal-to-noise-ratio of the Co 2p photoemission lines. Although the ensemble of characterization studies consistently show high phase purity and crystallinity, the observation of La-enriched surfaces may call into question the role of the B-site on the electrocatalytic properties of these materials.

Figure 5 compares the current densities at the disk ($j_D$, bottom panel) and the ring ($j_R$, top panel) of LaCrO₃, LaMnO₃, LaFeO₃, LaCoO₃ and LaNiO₃ electrodes at 1600 rpm and 0.010 V s⁻¹ in a O₂ saturated 0.1 M KOH solution. Current densities were calculated using the electrode geometrical area. Under the same conditions, the responses obtained for Pt/Etek and a Vulcan film are also shown. The onset potential for 20% wt. Pt/Etek catalysts is in agreement with previous studies in the literature.[19] The first striking observation is that the onset potential for ORR is rather similar for several oxides and the Vulcan film. This onset potential falls within the range of values reported in the literature for various carbon materials in alkaline media.[20] On the other hand, LaMnO₃ shows an onset potential significantly more positive, featuring a shoulder in the range between 0.75 and 0.85 V. As discussed further below, this feature is important in order to understand the high activity of LaMnO₃. The response observed for the Pt based

catalyst is consistent with the 4e$^-$ ORR pathway.[21] The angular rotation rate affects the overall current density in large portions of the potential range as illustrated for LaMnO$_3$, LaNiO$_3$ and Vulcan electrodes (no oxide catalysts) in the supporting information (Figures S5 and S6).

It is interesting to see that the magnitude of the ring and disc current densities for LaCrO$_3$, LaFeO$_3$ and LaNiO$_3$ electrodes are affected by the nature of the B-site. However, the ORR onset potential is very similar for all of these materials and very close to the onset potential for the Vulcan film. This behavior is consistent with the view that B-site does play a role on the catalytic activity of ORR, but primarily on the reduction of HO$_2^-$ (reactions 3 and 4).[22] The catalytic activity of perovskite materials in the HO$_2^-$ disproportionation reaction has been discussed in previous publications.[13a, 23]
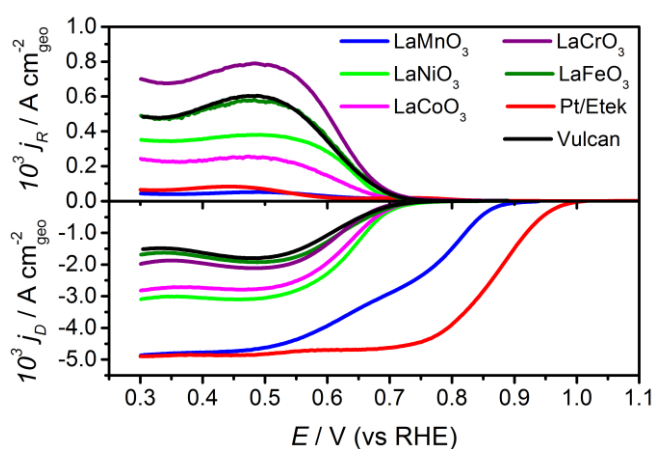


**Figure 5.** Disk current density ($j_D$) as a function of potential of Vulcan supported LaCrO$_3$, LaMnO$_3$, LaFeO$_3$, LaCoO$_3$ and LaNiO$_3$ electrodes at 1600 rpm in O$_2$-saturated 0.1 M KOH and a scan rate of 10 mV s$^{-1}$. The Pt-ring responses ($j_R$) were recorded by holding the potential at +1.1 V. The performance of the lanthanide catalysts are also contrasted with those of the carbon support (Vulcan) and the commercial Pt/Etek catalyst.

Using the current values recorded at the disk and ring electrodes at 1600 rpm, the HO$_2^-$ yield as function of the electrode potential was calculated for each of the materials investigated (Figure S7). LaMnO$_3$ and Pt/Etek electrodes exhibit less than 7% HO$_2^-$ yield over the whole potential range, while the other perovskites exhibit a more substantial yield following the trend LaCrO$_3$ > LaFeO$_3$ > LaNiO$_3$ > LaCoO$_3$. This behavior shows that LaMnO$_3$ not only features a significantly more positive onset potential for ORR, but also a stronger tendency to the 4e$^-$ process (eq. 1). As shown in figure S8, decreasing the LaMnO$_3$ loading to 62.5 µg cm$^{-2}$ leads to a slight increase in the ring current density and a decrease in the diffusion limited disk current density. This behavior is expected as the overall contribution of the carbon support to the ORR increases with decreasing catalyst loading. However, in the potential range where ORR exclusively takes place at the LaMnO$_3$ particles (between 0.7 and 0.9 V), the ring current remains very small and independent of the oxide loading. This observation confirms that low HO$_2^-$ yields in the presence of LaMnO$_3$ are not related to catalyst loading.

Figure 6 exemplifies the dependence of the disc current ($i_D$) with the angular rotation ($\omega$) for LaMnO$_3$ and LaNiO$_3$ following the Koutecky-Levich formalism,

$$\frac{1}{i_D} = \frac{1}{i_k} + \frac{1}{i_L} = \frac{1}{i_k} + \frac{1}{0.62nAFcD^{2/3}v^{-1/6}\omega^{1/2}} \quad (5)$$

where $i_k$ and $i_L$ are the kinetically and mass transport limiting current. The latter parameter is dependent of the number of transferred electrons ($n$), oxygen diffusion coefficient ($D$=1.9×10$^{-5}$ cm$^2$ s$^{-1}$),[24] bulk oxygen concentration ($c$=1.2×10$^{-6}$ mol cm$^3$), kinematic viscosity ($v$=0.01 cm$^2$ s$^{-1}$). Other parameters in eq. 5 include the disc geometric area ($A$) and the Faraday constant ($F$). LaMnO$_3$ (figure 6a) exhibits a linear dependence in the potential range between 0.60 and 0.30 V, with a slope consistent with $n = 4$. The same slope can also be observed even at potentials close to 0.9 V and for LaMnO$_3$ loading as low as 62.5 µg cm$^{-2}$ (Figure S8). On the other hand, LaNiO$_3$ (figure 6b) shows a slight change of slope with increasing angular rotation rate; a behavior also seen for LaCrO$_3$, LaFeO$_3$ and LaCoO$_3$ (Figure S9). The change of slope can be linked to the dynamics of peroxide reduction at the catalyst surface considering a reaction path based on eqs. 2 and 3. Increasing rotation rates can decrease the probability of the second reduction step (eqs. 3), leading to a value of $n$ closer to 2. Figure S10 shows the effective value of $n$ estimated from the ratio between the ring and disc currents at 1600 rpm, evolving from values between 2 and 3 for the various oxides to a value of 4 for LaMnO$_3$ and Pt.

Several models have been developed for quantitative analysis of ORR kinetics employing RRDE.[16, 25] One of the simplest approaches was proposed by Damjanovic et al., correlating the ring and disc currents in order to establish the ORR pathway.[16] As illustrated in scheme 1, the direct 4e$^-$ oxygen reduction pathway is defined in terms of negligible population of HO$_2^-$ within the experimental time scale. On the other hand, the so-called indirect path involves a measurable population of HO$_2^-$ which can be detected at the ring. In scheme 1, only species within the reaction layer (denoted with *) can undergo electron transfer with either the disc or ring, as opposed to bulk (b) species. The phenomenological rate constants associated with direct ($k_1$) and indirect ($k_2$) pathways contain contributions from a variety of parameters such as particle size, catalyst loading, intermediate coverage, rate constant of elementary electron transfer steps and so forth. Full details on the assessment of the various rate constants are given in the Supporting Information (Equations S3 to S9). We shall focus on the value of $k_1$ as this is the relevant parameter in the context of alkaline fuel cell applications. As described in the supporting information, $k_1$ is directly extracted from the values of $i_D$, $i_R$ and N.
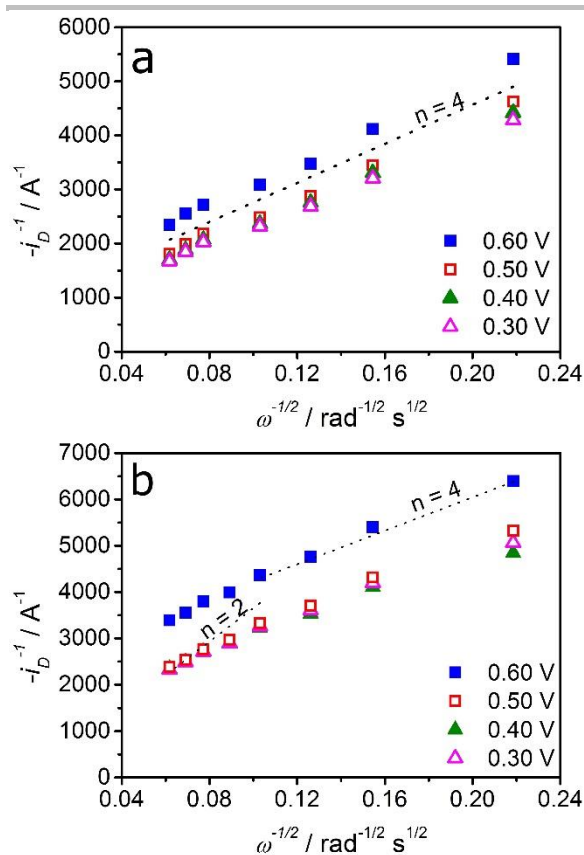
**Figure 6.** Koutecky-Levich plots for ORR on LaMnO$_3$ (a) and LaNiO$_3$ (b) electrodes in O$_2$-saturated 0.1 M KOH at different potentials. Dotted lines represent the characteristic slopes for the two different reactions.

**Scheme 1.** Simplified ORR mechanism illustrating the direct and indirect pathways with the associated phenomenological rate constants $k_1$, $k_2$ and $k_3$. Subscripts b and * designate bulk and reaction layer, respectively.
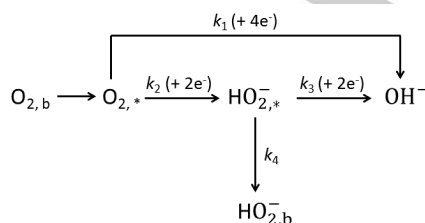


Figure 7a shows the potential dependence of $k_1$ for the various lanthanides. The phenomenological rate constants show an exponential increase as the potential decreases, with LaMnO$_3$ exhibiting measurable values at potentials more than 150 mV more positive than the other lanthanides. The potential dependence of this rate constant is similar for all oxides. Extrapolating the value of $k_1$ to 0.7 V allows establishing a comparison of the various oxides as exemplified in figure 7b. We have chosen this potential in order to minimize extrapolation of

the measure trends over large potential ranges. Figure 7b further emphasizes the fact that LaMnO$_3$ exhibit a unique activity towards ORR. Indeed, small differences in the overall magnitude of $k_1$ can be observed for the Fe, Co and Ni based oxides, while LaCrO$_3$ exhibit significantly lower values. The ratio $k_2 / k_1$ is shown in Figure S11 of the Supporting Information. The trend is the opposite of the one observed for $k_1$, with LaCrO$_3$ exhibiting three orders of magnitude higher ratio than LaMnO$_3$. On the other hand, the values for the phenomenological $k_3$ constant were in the range of $10^{-3}$ to $10^{-4}$ cm s$^{-1}$ for all oxides over the potential range investigated (figure S11).
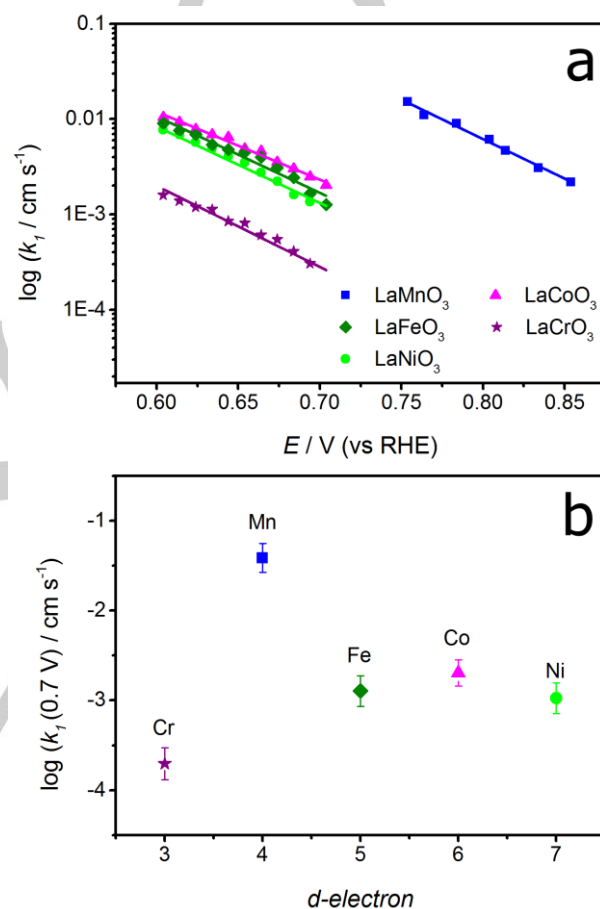


**Figure 7.** Phenomenological rate constant for the direct 4e$^-$ process ($k_1$) calculated for the different materials in 0.1 M KOH employing the Damjanovic's method (a). $k_1$ at 0.7 V versus the number $d$-electron in the B-site metal (b). As ORR onset potential is very different in the case LaMnO$_3$, the value of $k_1$(0.7 V) was obtained from extrapolating the trend in figure 7a. These plots demonstrate that the reactivity of LaMnO$_3$ towards the 4e$^-$ ORR is significantly higher which cannot be directly correlated to B-site orbital occupancy.

As shown in figure 7b, the value of $k_1$ do not correlate with the number of $d$-electrons of the B-site. Furthermore, the single e$_g$ orbital occupancy descriptor fails to describe this trend.[8b] LaFeO$_3$ has double e$_g$ occupancy, while LaCoO$_3$, LaNiO$_3$ and LaMnO$_3$ have single occupancy, and LaCrO$_3$ exhibits empty e$_g$ orbitals.[8a, 26] It could be argued that the vacant e$_g$ orbitals in LaCrO$_3$ determines the low performance of this material for direct ORR,

yet it is clear that the high activity of $LaMnO_3$ arises from an entirely different physical parameter. In order to rationalize this activity trend, we shall focus our attention onto the redox properties of the perovskite oxides in absence of $O_2$.

Figure 8a contrasts cyclic voltammograms of the various Vulcan supported oxides in Argon-saturated 0.1 M KOH solution at 10 mV s$^{-1}$. No clear redox responses can be observed for $LaFeO_3$, $LaCoO_3$ or $LaCrO_3$ within the potential window relevant to ORR reaction. $LaNiO_3$ does exhibit a reduction wave with an onset located around 0.2 V more negative than the onset of ORR at the carbon support. Figure 8a also shows that $LaMnO_3$ exhibits two reduction steps with peaks centered at 0.90 and 0.45 V. These changes of oxidation state occur in the same potential range reported for the reduction of $Mn_2O_3$ to $Mn_3O_4$ and from $Mn_3O_4$ to $Mn(OH)^+$, respectively.[19c, 27] It is clear that only $LaMnO_3$ exhibits clearly changes in redox states at potentials more positive than the onset of ORR at the carbon support. Consequently, we postulate that the higher activity with respect to other lanthanides is directly linked to changes in Mn oxidation state close to the ORR formal redox potential.
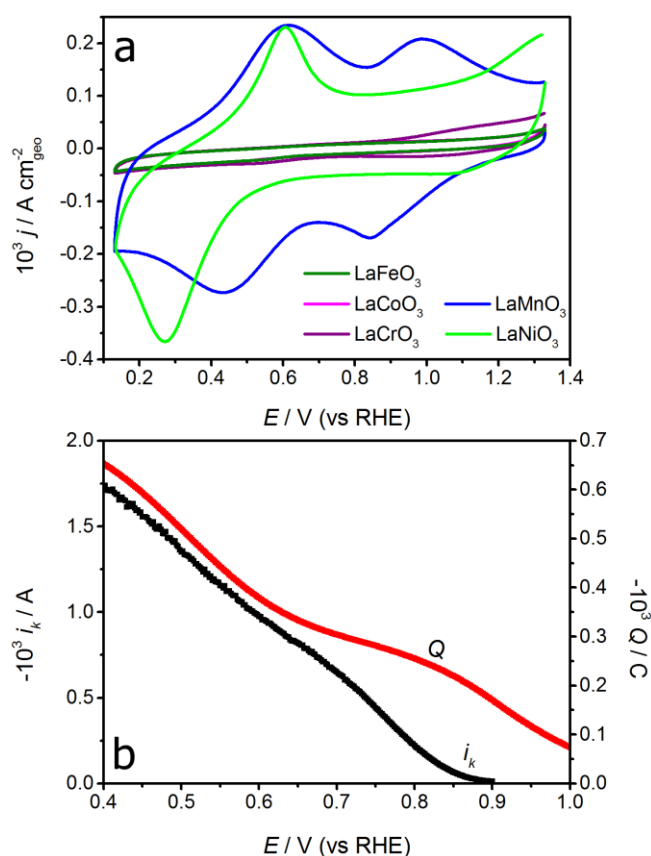


**Figure 8.** Cyclic voltammograms of the Vulcan supported oxides in Ar-saturated 0.1 M KOH solution at 10 mV s$^{-1}$. Oxide loading is identical to those reported in figure 5. The responses of $LaCoO_3$ and $LaCrO_3$ are superimposed and cannot be clearly differentiated in this scale (a). Potential dependence of $i_k$ and of the charge associated with redox processes at $LaMnO_3$ (b).

The charge associated with the reduction steps at $LaMnO_3$ as a function of the applied potential is displayed in figure 8b. On average, the charge obtained across the potential range is consistent with approximately 2% of the Mn population per nanoparticle undergoing an oxidation state for $Mn^{3+}$ to $Mn^{2+}$. However, integration of these voltammetric responses is somewhat complicated by the presence of a large capacitive current also observed in the case of $LaNiO_3$. This interesting observation has already been reported by Stevenson and co-workers, linking this phenomenon to anion ($OH^-$) intercalation.[28] Figure S11 graphically exemplifies the background subtraction implemented for estimating the reduction charge. It should also be mentioned that the faradaic charges associated with the anodic and cathodic cycles are very similar, while the responses appear stable within a number of cycles in this potential range. These results suggest that the stability of these materials is not significantly compromised within the time-scale of these experiments.

Figure 8b also shows the change in the kinetically limited current ($i_k$) obtained from Koutecky-Levich analysis of the $LaMnO_3$. Interestingly, the reduction charge and $i_k$ show similar trends as a function of the applied potential except at values more positive than 0.9 V. There is a sizeable increase of the charge at potentials above 0.9 V which does not manifest itself in clear changes in $i_k$. It should be considered that a variety of processes can be contributing to the electrochemical responses in this potential range as recently reviewed by Shao-Horn and co-workers, highlighting aspects related to crystallite size and phases.[29] Ahmad *et al.* estimated differences in $O_2$ binding energies as large as 2 eV for different Mn sites as a result of Janh-Teller distortions in orthorhombic phases.[30] Furthermore, processes such as $OH^-$ intercalation mentioned above,[28] may also contribute to the current responses in this potential range. Consequently, additional studies are required in order to rationalize the various processes contributing to the voltammetric responses and to identify the species responsible for the strong changes in $i_k$.

Finally, an interesting point to assess is the performance of $LaMnO_3$ with respect to Pt/Etek, considering that both materials essentially operate through the 4$e^-$ reduction mechanism. Table S2 summarizes the main activity descriptors obtained from the RRDE responses, including $i_k$ at 0.90 V. This parameter is commonly used as activity descriptor, avoiding controversial extrapolations over large potential ranges (Tafel plots).[21c] Table S2 shows values of $(2.4\pm0.4)\cdot10^{-4}$ and $(1.2\pm0.2)\cdot10^{-5}$ A for Pt and $LaMnO_3$ catalysts, which reflect the difference in the current-potential relationship between Pt/Etek and $LaMnO_3$ seen in figure 5. However, it should be considered that catalyst loadings and particle size are significantly different for both materials (see Table S1 of the Supporting information). Normalizing $i_k$(0.90 V) by SSA (see footnote 2 and table S2), we estimate $(8.0\pm1.4)\cdot10^{-6}$ A cm$^{-2}$ for Pt and $(1.5\pm0.1)\cdot10^{-6}$ A cm$^{-2}$ for $LaMnO_3$. The value obtained for Pt/Etek is consistent with values reported in the literature under alkaline conditions.[21a, 21c] On the other hand, we obtained kinetic currents normalized by mass comparable to recent reports.[27b, 29] In this analysis, it ought to be considered that significant levels of A-site segregation can occur in this material according to our XPS analysis, as well as by others.[31] The charge estimated from the voltammetric responses (see fig. 8b and S11)

over the entire potential range can be used as an indication of the number density of surface Mn sites. In the case of Pt nanostructures, the number density of surface Pt atoms can be estimated from voltammetric parameters such as hydrogen desorption, oxide reduction and adsorbed CO oxidation peaks (see figure S11). Normalizing the kinetic current at 0.90 V by the number of electroactive surface sites, we obtain values of the order of $(2.9\pm0.3)\cdot10^{-21}$ and $(1.3\pm0.4)\cdot10^{-20}$ A for $LaMnO_3$ and Pt-Etek, respectively. The error margins in these estimation also take into account uncertainty in the background subtraction. This analysis reveals that surface Mn(III) sites are significantly more active than previously considered, in particular if kinetic descriptors are only normalized by mass or specific surface area.

The ensemble of experimental observations strongly point towards changes in the oxidation state of Mn(III) sites as the key process leading to ORR, including oxygen bond breaking. We believe these observations are crucially important for rationalizing the properties of these materials. Parameters such as oxygen adsorption energies at surfaces in their equilibrium electronic configuration only represent one aspect of the physics involved in these complex reactions. In the broader context of oxygen electrocatalysis, these results are also consistent with recent studies showing that the most active catalysts for the oxygen evolution reaction do exhibit changes in redox states under operational conditions.[32] The challenge remains in identifying the most active Mn sites and developing synthetic routes to overexpress these sites. For example, selecting the appropriate A-site may not only lead to an optimum charge density at the Mn sites,[33] but also minimize its surface depletion.

## Conclusions

In this work, we have shown that $LaMnO_3$ exhibits unique activity towards the ORR which is linked to changes in oxidation state of the B-cation at potential close to the formal oxygen redox potential. Our investigations revealed that descriptors such as the number of d-electrons or $e_g$ orbital occupancy cannot rationalize the several orders of magnitude difference in activity between $LaMnO_3$ and several other lanthanides towards the 4$e^-$ reduction mechanism. To uncover this piece of information, quantitative electrochemical studies involving rotating ring-disc electrodes are performed in order to deconvolute the reaction pathways and to quantify their corresponding rate constants. Furthermore, quantitative analysis was enabled by the preparation of Vulcan supported oxides with high phase purity, crystallinity and nanoscale structure. Indeed, our versatile ionic liquid based approach allowed the facile synthesis of $LaCrO_3$, $LaMnO_3$, $LaFeO_3$, $LaCoO_3$ and $LaNiO_3$.

We provide conclusive evidences confirming that carbon supports play a major role in the ORR process, particularly in the case of $LaCrO_3$, $LaFeO_3$, $LaCoO_3$ and $LaNiO_3$. The ORR onset potential at these oxides overlaps with $HO_2^-$ generation at the carbon support. On the other hand, $LaMnO_3$ exhibited an onset potential for ORR significantly more positive than the other carbon supported oxides, with nearly 100% selectivity towards the 4$e^-$ reaction. This behavior translates into phenomenological electron rate constant for the 4$e^-$ process several orders of magnitude

higher in the case of $LaMnO_3$. The origin of this distinctive reactivity is associated with the electronic population of Mn (III) surface state with energy closely overlapping with the oxygen reduction energy. A key challenge is to identify the nature of the active Mn (III) state in order to develop synthetic methods capable of over-expressing this active site. Other results, to be reported elsewhere, show that this site can be affected by the oxygen content in the crystal structure as well as the properties of the A-site.

## Experimental Section

$LaCrO_3$, $LaMnO_3$, $LaFeO_3$, $LaCoO_3$ and $LaNiO_3$ particles were synthesized using an ionic liquid/cellulose system, based on a procedure reported elsewhere.[15] Briefly, 1 mL of 1 M aqueous solution of the metal precursors (nitrate salts) was added to a vial containing 1 mL of 1-ethyl-3-methylimiamidizolium acetate and heated at 80°C for 2 hours to promote water evaporation and precursor phase transfer. Dissolution of 100 mg of cellulose, acting as chelating agent, over the course of 15 minutes and subsequent calcination of the mixture at different temperatures for 2 hours produced the desired multicomponent metal oxide phase. The calcination temperature was set at 700°C for $LaMnO_3$, 800°C for $LaNiO_3$ and $LaCoO_3$, and 900°C for $LaFeO_3$ and $LaCrO_3$. The different calcination temperatures were established such that high levels of crystallinity are ensured, while minimizing the presence of secondary phases. Phase purity is the key parameter to control, requiring adjusting the crystallization temperature according to the thermochemistry of the B-precursor.

XRD was performed with a Bruker AXS D8 Advance diffractometer featuring a CuKα radiation source (λ = 0.154 nm). X-ray photoelectron spectra (XPS) were acquired with a Kratos Ultra Axis XPS system equipped with a delay-line detector (DLD). Core-level photoemission spectra were taken at room temperature in normal emission using a monochromatic Al Kα X-ray source (1486.7 eV). Single spectral regions were collected using 0.1 eV steps, 0.5 s collection time and 20 eV pass energy. The binding energies (BE) were referenced to the C 1s peak at 284.7 eV (not shown). The structure of the catalysis was also investigated with scanning (JEOL SEM 5600 LV) and transmission electron microscopy (JEOL JEM-1400Plus and JEOL JEM 2010). Samples for TEM were produced by placing 1 μL drops of the oxide particles dissolved in ethanol on a 3 mm diameter carbon-coated copper grid. Mean particle diameters were estimated from at least 100 nanoparticles per sample.

Electrochemical measurements were conducted using a rotating ring-disk electrode (RRDE) operated with an ALS Rotation Controller and an Ivium-CompactStat bipotentiostat. The RRDE consisted of a 4 mm diameter glassy carbon disk and a platinum ring with a 7 mm outer diameter. The RRDE collection efficiency was determined to be 0.42 employing ferrocenemethanol as redox probe. Pt foil and Hg/HgO (1 M NaOH, IJ Cambria) were used as counter and reference electrodes, respectively. We have performed experiments with different counter-electrodes including graphite and Au rods, confirming that the responses are not affected by contamination from the counter-electrode (see Supporting Information figure S12). Furthermore, there is no time dependence in the performance of any of the catalysts which may suggest any aging issues within the time-scale of the studies. Every set of experiments was carried out with fresh electrolyte solutions. The reference electrode, which was calibrated against the reversible hydrogen electrode (RHE), was placed in a separate compartments connected by a Luggin capillary. To facilitate the discussion, all potentials herein are quoted against RHE. Measurements were carried out in a 0.1 M KOH solution purged either with high purity Ar or $O_2$ (BOC). The uncompensated resistance estimated by electrochemical impedance spectroscopy was typically 70 Ω. Under the current experimental conditions, effects from IR compensation are

negligible. Every set of experiments was carried out with fresh electrolyte solutions.

Electrodes were prepared by a two-step drop-casting process. Controlled amounts of an ink containing Vulcan and $Na^+$-exchanged Nafion® (5 wt.%, Sigma-Aldrich) are deposited onto the glassy carbon disk, followed by drop-casting an aqueous suspension of the oxide. Keeping the oxide and carbon in separate suspensions allows visualizing the homogeneity of the suspensions prior to the drop-casting steps. The final loading onto each electrode was 250 $\mu g_{OXIDE}$ cm$^{-2}$, 50 $\mu g_{VULCAN}$ cm$^{-2}$ and 50 $\mu g_{NAFION}$ cm$^{-2}$. This catalyst loading is comparable to other works in the literature.[6b, 34] This leads to an effective Nafion film thickness of less than 0.5 μm (see footnote 1). Such thin Nafion layers ensures that any potential film diffusion resistance remain negligible.[21a, 35] Finally, 20 wt.% Pt supported on Vulcan XC-72 (Pt/Etek) was used as a benchmark in these studies. The loading of the catalysts at the electrode surface was 250 $\mu g_{Pt}$ cm$^{-2}$, 1000 $\mu g_{CARBON}$ cm$^{-2}$ and 50 $\mu g_{NAFION}$ cm$^{-2}$. We performed a large number of experiments employing $LaMnO_3$, with different catalyst loading, to confirm the reproducibility and self-consistency of our approach (see supporting information S8). Values reported here were obtained from averaging the responses of 3 to 6 different catalysts layer of each material prepare on different days.

## Footnotes

$^1$Calculated as $\tau$ = m/($\pi r^2 \rho$), being *m* the mass of Nafion in the electrode and $\rho$ the film density assumed to be 2.0 g cm$^{-3}$.

$^2$SSA was calculated assuming that the oxide particles are spherical, by the ratio SSA (m$^2$ g$^{-1}$) = 6×10$^3$ /$\rho d$.

## Acknowledgements

**Keywords:** Perovskite nanoparticles • Oxygen Reduction Reaction • Electrocatalysis • $LaMnO_3$ • Carbon Support

[1] S. Park, Y. Shao, J. Liu, Y. Wang, Energ. Environ. Sci. 2012, 5, 9331-9344.

[2] C. Song, J. Zhang, in PEM Fuel Cell Electrocatalysts and Catalyst Layers (Ed.: J. Zhang), Springer London, **2008**, pp. 89-134.

[3] N. M. Marković, T. J. Schmidt, V. Stamenković, P. N. Ross, Fuel Cells 2001, 1, 105-116.

[4] a) B. Wang, J. Power Sources 2005, 152, 1-15; b) F. Jaouen, E. Proietti, M. Lefevre, R. Chenitz, J.-P. Dodelet, G. Wu, H. T. Chung, C. M. Johnston, P. Zelenay, Energ. Environ. Sci. 2011, 4, 114-130; c) Z. Chen, D. Higgins, A. Yu, L. Zhang, J. Zhang, Energ. Environ. Sci. 2011, 4, 3167-3192.

[5] a) J. Greeley, I. E. L. Stephens, A. S. Bondarenko, T. P. Johansson, H. A. Hansen, T. F. Jaramillo, J. Rossmeisl, I. Chorkendorff, J. K. Nørskov, Nat. Chem. 2009, 1, 552-556; b) J. Rossmeisl, A. Logadottir, J. K. Nørskov, Chem. Phys. 2005, 319, 178-184.

[6] a) J. Sunarso, A. A. J. Torriero, W. Zhou, P. C. Howlett, M. Forsyth, J. Phys. Chem. C 2012, 116, 5827-5834; b) J. Suntivich, H. A. Gasteiger, N. Yabuuchi, Y. Shao-Horn, J. Electrochem. Soc. 2010, 157, B1263-B1268; c) T. Poux, F. S. Napolskiy, T. Dintzer, G. Kéranguéven, S. Y.

[7] Istomin, G. A. Tsirlina, E. V. Antipov, E. R. Savinova, Catal. Today 2012, 189, 83-92.

[7] J. O. M. Bockris, T. Otagawa, J. Electrochem. Soc. 1984, 131, 290-302.

[8] a) Y. Wang, H.-P. Cheng, J. Phys. Chem. C 2013, 117, 2106-2112; b) J. Suntivich, H. A. Gasteiger, N. Yabuuchi, H. Nakanishi, J. B. Goodenough, Y. Shao-Horn, Nat. Chem. 2011, 3, 647-651; c) Y.-L. Lee, J. Kleis, J. Rossmeisl, Y. Shao-Horn, D. Morgan, Energ. Environ. Sci. 2011, 4, 3966-3970.

[9] F. Calle-Vallejo, N. G. Inoglu, H.-Y. Su, J. I. Martinez, I. C. Man, M. T. M. Koper, J. R. Kitchin, J. Rossmeisl, Chem. Sci. 2013, 4, 1245-1249.

[10] a) J. Druce, H. Tellez, M. Burriel, M. D. Sharp, L. J. Fawcett, S. N. Cook, D. S. McPhail, T. Ishihara, H. H. Brongersma, J. A. Kilner, Energ. Environ. Sci. 2014; b) M. Burriel, S. Wilkins, J. P. Hill, M. A. Munoz-Marquez, H. H. Brongersma, J. A. Kilner, M. P. Ryan, S. J. Skinner, Energ. Environ. Sci. 2014, 7, 311-316; c) J. A. Kilner, M. Burriel, Annu. Rev. Mat. Res. 2014, 44, 365-393; d) H. Téllez, J. Druce, Y.-W. Ju, J. Kilner, T. Ishihara, Int. J. Hydrogen Energy 2014, 39, 20856-20863; e) M. L. Reinle-Schmitt, C. Cancellieri, A. Cavallaro, G. F. Harrington, S. J. Leake, E. Pomjakushina, J. A. Kilner, P. R. Willmott, Nanoscale 2014, 6, 2598-2602; f) J. Chen, M. Döbeli, D. Stender, K. Conder, A. Wokaun, C. W. Schneider, T. Lippert, Applied Physics Letters 2014, 105, 114104.

[11] a) M. Appel, A. J. Appleby, Electrochim. Acta 1978, 23, 1243-1246; b) D.-W. Wang, D. Su, Energ. Environ. Sci. 2014, 7, 576-591.

[12] a) W. G. Hardin, D. A. Slanac, X. Wang, S. Dai, K. P. Johnston, K. J. Stevenson, J. Phys. Chem. Lett. 2013, 4, 1254-1259; b) W. G. Hardin, J. T. Mefford, D. A. Slanac, B. B. Patel, X. Wang, S. Dai, X. Zhao, R. S. Ruoff, K. P. Johnston, K. J. Stevenson, Chem. Mater. 2014, 26, 3368-3376.

[13] a) T. Poux, A. Bonnefont, A. Ryabova, G. Kerangueven, G. A. Tsirlina, E. R. Savinova, Phys. Chem. Chem. Phys. 2014, 16, 13595-13600; b) T. Poux, A. Bonnefont, G. Kéranguéven, G. A. Tsirlina, E. R. Savinova, ChemPhysChem 2014, 15, 2108-2120.

[14] S. Malkhandi, P. Trinh, A. K. Manohar, K. C. Jayachandrababu, A. Kindler, G. K. Surya Prakash, S. R. Narayanan, J. Electrochem. Soc. 2013, 160, F943-F952.

[15] a) V. Celorrio, K. Bradley, O. J. Weber, S. R. Hall, D. J. Fermín, ChemElectroChem 2014, 1, 1667-1671; b) D. C. Green, S. Glatzel, A. M. Collins, A. J. Patil, S. R. Hall, Adv. Mater. 2012, 24, 5767-5772.

[16] A. Damjanovic, M. A. Genshaw, J. O. Bockris, M., J. Chem. Phys. 1966, 45, 4057-4059.

[17] J. Rodríguez-Carvajal, M. Hennion, F. Moussa, A. H. Moudden, L. Pinsard, A. Revcolevschi, Physical Review B 1998, 57, R3189-R3192.

[18] a) M. F. Sunding, K. Hadidi, S. Diplas, O. M. Løvvik, T. E. Norby, A. E. Gunnæs, J. Electron. Spectrosc. Relat. Phenom. 2011, 184, 399-409; b) M. C. Álvarez-Galván, V. A. de la Peña O'Shea, G. Arzamendi, B. Pawelec, L. M. Gandía, J. L. G. Fierro, Appl. Catal., B 2009, 92, 445-453; c) K. Bolwin, W. Schnurnberger, G. Schiller, Z. Physik B - Condensed Matter 1988, 72, 203-209.

[19] a) Y. Gorlin, T. F. Jaramillo, J. Am. Chem. Soc. 2010, 132, 13612-13614; b) Y. Gorlin, C.-J. Chung, D. Nordlund, B. M. Clemens, T. F. Jaramillo, ACS Catalysis 2012, 2, 2687-2694; c) H.-Y. Su, Y. Gorlin, I. C. Man, F. Calle-Vallejo, J. K. Norskov, T. F. Jaramillo, J. Rossmeisl, Phys. Chem. Chem. Phys. 2012, 14, 14010-14022.

[20] a) G. Zhutaeva, V. Bogdanovskaya, E. Davydova, L. Kazanskii, M. Tarasevich, J. Solid State Electrochem. 2014, 18, 1319-1334; b) K. Tammeveski, K. Kontturi, R. J. Nichols, R. J. Potter, D. J. Schiffrin, J. Electroanal. Chem. 2001, 515, 101-112.

[21] a) U. A. Paulus, T. J. Schmidt, H. A. Gasteiger, R. J. Behm, J. Electroanal. Chem. 2001, 495, 134-145; b) T. J. Schmidt, V. Stamenkovic, J. P. N. Ross, N. M. Markovic, Phys. Chem. Chem. Phys. 2003, 5, 400-406; c) H. A. Gasteiger, S. S. Kocha, B. Sompalli, F. T. Wagner, Appl. Catal. B 2005, 56, 9-35.

[22] F. d. r. Jaouen, J. Phys. Chem. C 2009, 113, 15433-15443.

[23] a) Y. N. Lee, R. M. Lago, J. L. G. Fierro, J. González, Appl. Catal., A 2001, 215, 245-256; b) H. Falcón, R. E. Carbonio, J. L. G. Fierro, J. Catal. 2001, 203, 264-272; c) A. Ariafard, H. R. Aghabozorg, F. Salehirad, Catal. Commun. 2003, 4, 561-566.

[24]    A. J. Bard, Electrochemical methods : fundamentals and applications / Allen J. Bard, Larry R. Faulkner, Wiley, New York, **1980**.

[25]    a) H. S. Wroblowa, P. Yen Chi, G. Razumney, J. Electroanal. Chem. 1976, 69, 195-201; b) A. J. Appleby, M. Savy, J. Electroanal. Chem. 1978, 92, 15-30; c) R. W. Zurilla, R. K. Sen, E. Yeager, J. Electrochem. Soc. 1978, 125, 1103-1109; d) V. S. Bagotzky, N. A. Shumilova, G. P. Samoilov, E. I. Khrushcheva, Electrochim. Acta 1972, 17, 1625-1635; e) N. A. Anastasijević, V. Vesović, R. R. Adžić, J. Electroanal. Chem. 1987, 229, 305-316.

[26]    a) B. W. Veal, D. J. Lam, J. Appl. Phys. 1978, 49, 1461-1462; b) U. Maitra, B. S. Naidu, A. Govindaraj, C. N. R. Rao, PNAS 2013.

[27]    a) M. Wiechen, H.-M. Berends, P. Kurz, Dalton T. 2012, 41, 21-31; b) G. Kéranguéven, S. Royer, E. Savinova, Electrochem. Commun. 2015, 50, 28-31.

[28]    J. T. Mefford, W. G. Hardin, S. Dai, K. P. Johnston, K. J. Stevenson, Nat Mater 2014, 13, 726-732.

[29]    K. A. Stoerzinger, M. Risch, B. Han, Y. Shao-Horn, ACS Catalysis 2015, 5, 6021-6031.

[30]    E. A. Ahmad, V. Tileli, D. Kramer, G. Mallia, K. A. Stoerzinger, Y. Shao-Horn, A. R. Kucernak, N. M. Harrison, J. Phys. Chem. C 2015, 119, 16804-16810.

[31]    W. Lee, J. W. Han, Y. Chen, Z. Cai, B. Yildiz, J. Am. Chem. Soc. 2013, 135, 7909-7925.

[32]    a) D. Friebel, M. W. Louie, M. Bajdich, K. E. Sanwald, Y. Cai, A. M. Wise, M.-J. Cheng, D. Sokaras, T.-C. Weng, R. Alonso-Mori, R. C. Davis, J. R. Bargar, J. K. Nørskov, A. Nilsson, A. T. Bell, J. Am. Chem. Soc. 2015, 137, 1305-1313; b) K. Sardar, E. Petrucco, C. I. Hiley, J. D. B. Sharman, P. P. Wells, A. E. Russell, R. J. Kashtiban, J. Sloan, R. I. Walton, Angew. Chem. 2014, 126, 11140-11144; c) T. Binninger, R. Mohamed, K. Waltar, E. Fabbri, P. Levecque, R. Kötz, T. J. Schmidt, Scientific Reports 2015, 5, 12167.

[33]    a) K. A. Stoerzinger, W. Lü, C. Li, Ariando, T. Venkatesan, Y. Shao-Horn, J. Phys. Chem. Lett. 2015, 6, 1435-1440; b) K. A. Stoerzinger, M. Risch, J. Suntivich, W. M. Lu, J. Zhou, M. D. Biegalski, H. M. Christen, Ariando, T. Venkatesan, Y. Shao-Horn, Energ. Environ. Sci. 2013, 6, 1582-1588.

[34]    a) J. Suntivich, E. Perry, H. Gasteiger, Y. Shao-Horn, Electrocatalysis 2013, 4, 49-55; b) E. Fabbri, R. Mohamed, P. Levecque, O. Conrad, R. Kötz, T. J. Schmidt, ACS Catalysis 2014, 4, 1061-1070.

[35]    T. J. Schmidt, H. A. Gasteiger, G. D. Stäb, P. M. Urban, D. M. Kolb, R. J. Behm, J. Electrochem. Soc. 1998, 145, 2354-2358.

**Entry for the Table of Contents** (Please choose one layout)

Layout 1:

## ARTICLE

Detailed electrochemical analysis of carbon supported lanthanide perovskites reveals that $LaMnO_3$ is orders of magnitude more active towards the 4-electron oxygen reduction under alkaline conditions. The origin of the reactivity is linked to changes in the redox state of the Mn(III) sites.
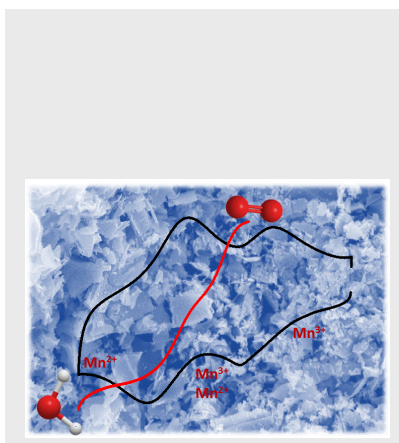
*Verónica Celorrio, Ellie Dann, Laura Calvillo,David J. Morgan, Simon R. Hall, and David J. Fermín\**

***Page No. – Page No.***

**Oxygen Reduction at Carbon Supported Lanthanides: The Role of the B-site**